Effect of Co doping on the structural, optical and magnetic properties of ZnO nanoparticles

Effect of Co doping on the structural, optical and magnetic properties of ZnO nanoparticles

J Hays[1]**, K M Reddy**[1]**, N Y Graces**[2]**, M H Engelhard**[3]**, V Shutthanandan**[3]**,
M Luo**[2]**, C Xu**[2]**, N C Giles**[2]**, C Wang**[3]**, S Thevuthasan**[3] **and A Punnoose**[1,4]

[1] Department of Physics, Boise State University, Boise, ID 83725-1570, USA
[2] Department of Physics, West Virginia University, Morgantown, WV 26506-6315, USA
[3] Environmental Molecular Sciences Laboratory, Pacific Northwest National Laboratory, Richland, WA 99352, USA

E-mail: apunnoos@boisestate.edu

Abstract

We report the results of a detailed investigation of sol–gel-synthesized nanoscale $Zn_{1-x}Co_xO$ powders processed at $350\,^{\circ}C$ with $0 \leqslant x \leqslant 0.12$ to understand how the structural, morphological, optical and magnetic properties of ZnO are modified by Co doping, in addition to searching for the theoretically predicted ferromagnetism. With x increasing to 0.03, both lattice parameters a and c of the hexagonal ZnO decreased, suggesting substitutional doping of Co at the tetrahedral Zn^{2+} sites. For $x > 0.03$, these trends reversed and the lattice showed a gradual expansion as x approached 0.12, probably due to additional interstitial incorporation of Co. Raman spectroscopy measurements showed a rapid change in the ZnO peak positions for $x > 0.03$, suggesting significant disorder and changes in the ZnO structure, in support of additional interstitial Co doping possibility. Combined x-ray photoelectron spectroscopy (XPS), electron paramagnetic resonance spectroscopy, photoluminescence spectroscopy and diffuse reflectance spectroscopy showed clear evidence for tetrahedrally coordinated high-spin Co^{2+} ions occupying the lattice sites of ZnO host system, which became saturated for $x > 0.03$. Magnetic measurements showed a paramagnetic behaviour in $Zn_{1-x}Co_xO$ with increasing antiferromagnetic interactions as x increased to 0.10. Surprisingly, a weak ferromagnetic behaviour was observed for the sample with $x = 0.12$ with a characteristic hysteresis loop showing a coercivity $H_c \sim 350$ Oe, 25% remanence M_r, a low saturation magnetization $M_s \sim 0.04$ emu g^{-1} and with a Curie temperature $T_c \sim 540$ K. The XPS data collected from $Zn_{1-x}Co_xO$ samples showed a gradual increase in the oxygen concentration, changing the oxygen-deficient undoped ZnO to an excess oxygen state for $x = 0.12$. This indicates that such high Co concentrations and appropriate oxygen stoichiometry may be needed to achieve adequate ferromagnetic exchange coupling between the incorporated Co^{2+} ions.

[4] Author to whom any correspondence should be addressed.

1. Introduction

Oxygen-deficient zinc oxide is an excellent n-type semiconductor with a wide band gap of 3.4 eV and a large exciton binding energy of 60 meV [1, 2]. For these reasons, ZnO is used in a wide variety of applications, including opto-electronic devices [3–6], catalysis [7], light-emitting diodes (LEDs) [8], thermoelectric devices [9], varistors [10, 11], flat panel displays [11] and surface acoustic wave devices [12]. Recent theoretical predictions [13–18] proposed transition metal (TM)-doped ZnO as one of the most promising candidates for room-temperature ferromagnetism (RTFM). Additionally, the excellent optical transparency of ZnO and the possibility of band gap engineering through TM doping strongly encourages the exploration of the magneto-optical properties of the TM-doped ZnO system [19, 20] which might lead to the development of novel magneto-optoelectronic devices [21–23].

A promising way to produce magnetic functionality in existing semiconductors is to dope them with magnetically active transition metals. Electronic structure calculations by Sato and Yoshida [15–17] led to two self-consistent solutions for the TM ions incorporated in dilute magnetic semiconductors (DMSs): (i) a ferromagnetic (FM) state stabilized by the double exchange interaction between the moments via the hopping of itinerant d electrons between the TM neighbours, and (ii) a spin glass (SG) state of randomly oriented magnetic moments dominated by antiferromagnetic (AF) superexchange interactions. The stability of the FM state over the SG state depends on the difference between the total energies of the two states, and this directly corresponds to the ordering temperature T_c. Among the II–VI compounds, ZnO is the most favourable system for RTFM since it shows a positive energy difference for V, Cr, Fe, Co or Ni doping and negative energy difference only for Mn doping. This indicates that V-, Cr-, Fe-, Co- or Ni-doped ZnO might directly stabilize an FM state while Mn-doped ZnO might form an SG state. Sato and Yoshida [15–17] have further shown that the magnetic properties of TM-doped ZnO can be varied systematically by changing the carrier concentration. Interestingly, they propose that hole doping could stabilize an FM state for Mn-doped ZnO. On the other hand, hole doping favours an SG state in all the other TM-doped ZnO systems whereas electron doping stabilizes the FM state. The development of ferromagnetism in semiconductors was also theoretically predicted by other groups [13, 14, 18].

The extensive theoretical work and predictions of high-temperature ferromagnetism in TM-doped ZnO stimulated an unprecedented amount of experimental studies in this system in general [24–28] and with Co doping in particular [28–41]. Experimental observation of ferromagnetism in these systems has been quite mixed. Several groups [28, 29, 32–42] have observed ferromagnetism in $Zn_{1-x}Co_xO$, while other groups [30, 31] have observed no such ferromagnetism in similar samples. Proposals for the origin of the observed ferromagnetism in $Zn_{1-x}Co_xO$ have been controversial, with numerous reports supporting the possibilities of both intrinsic mechanisms such as carrier-mediated ferromagnetism [22, 23, 33, 38] and the spin-split donor impurity band model [40], as well as extrinsic magnetic-impurity-cluster-driven mechanisms [29]. Experimental observations of metallic Co nanoparticles and clusters have been reported in some samples prepared by vacuum-based fabrication techniques [29]. It is therefore imperative to develop ferromagnetism in $Zn_{1-x}Co_xO$ prepared by new synthesis methods that would intrinsically exclude the formation of such magnetically active impurity phases in order to understand the actual origin of the observed ferromagnetism. Motivated by these reasons, we carried out a detailed investigation of $Zn_{1-x}Co_xO$ prepared by a sol–gel-based chemical method in air which would disallow the formation of ferromagnetic Co clusters. Any impurity phases, if formed, would be the oxides of Co which are all AF with Néel temperatures (T_N) below room temperature.

2. Experimental details

Zinc acetate, cobalt nitrate, and sodium hydroxide in suitable amounts, were added to deionized water to produce solutions with molarities of 0.25, 0.05, and 0.50 M respectively. Each sample was prepared by reacting the 0.05 M cobalt nitrate and 0.25 M zinc acetate solutions (molar ratio of $x = \frac{Co}{Co+Zn}$) with the 0.50 M sodium hydroxide solution. The resulting precipitate was washed to remove any water soluble by-products and annealed for 2 h at 350 °C to obtain $Zn_{1-x}Co_xO$. A rotary pump was used to reduce the air pressure in the annealing chamber to $\sim 10^{-3}$ Torr. To obtain more insight into possible Co impurity phases which might form under these synthesis conditions, pure Co oxide (Co_3O_4) samples were also prepared following identical synthesis procedures without using any Zn precursor.

The Co doping concentrations were determined by particle-induced x-ray emission (PIXE) measurements carried out in the accelerator facility at Pacific Northwest National Laboratory. However, the exact Co concentration was lower than the nominal concentration. The powder samples were first mixed with a very small amount of polyvinyl alcohol and then pelletized using a hand-operated press. The samples were then irradiated with a 2.0 MeV He^+ ion beam and the x-rays emitted during the de-excitation process within the atoms were analysed using an x-ray spectrometer.

X-ray diffraction (XRD) spectra were recorded at room temperature on a Phillips X'Pert x-ray diffractometer with a Cu Kα source ($\lambda = 1.5418$ Å) in Bragg–Brentano geometry. The loose powder samples were levelled in the sample holder to ensure a smooth surface and mounted on a fixed horizontal sample plane. Data analyses were carried out using profile fits of selected individual XRD peaks.

Photoluminescence (PL) measurements of the ZnO powders were performed from 4.8 to 300 K. The powders were pressed between sapphire plates with the edges then sealed with rubber cement. These samples were mounted on molybdenum plates and placed in a Janis SuperVaritemp dewar for cooling to liquid helium temperatures. The PL data were taken in near-backscattering geometry using a 0.64 m monochromator and a GaAs photomultiplier tube operating in photon-counting mode. The excitation wavelength was 325 nm (He–Cd laser) and the incident power density on the sample surface was about 1 W cm^{-2}. The data shown here have been corrected for the wavelength-dependent intensity response of the detection system using a calibrated white-light source.

Raman data were taken using a Jobin-Yvon U-1000 micro-Raman system with an Olympus BH-2 microscope. Data were taken using a backscattering geometry from the powder samples, which were pressed onto a plate and positioned below the objective lens. The emission signal was detected using a GaAs photomultiplier and photon-counting electronics. The 514.5 nm output from an argon ion laser was used. The power density on the sample surface was about 25 kW cm^{-2}. Photoluminescence data using the 514.5 nm excitation were also acquired using the micro-Raman system.

Electron paramagnetic resonance (EPR) measurements of the powder samples were performed. Small amounts (~ 40 mg) of each powder were placed in quartz tubes and inserted into the microwave cavity of a Bruker EMX system. The sample temperature was maintained by an Oxford liquid helium flow system. The data shown here were taken at 10 K using a 1 G modulation amplitude.

High-resolution transmission electron microscopy (TEM) analysis was carried out with a JEOL JEM 2010 microscope with a specified point-to-point resolution of 0.194 nm. The operating voltage of the microscope was 200 kV. All images were digitally recorded with a slow-scan CCD camera (image size 1024 × 1024 pixels), and image processing was carried out using the Digital Micrograph software from Gatan (Pleasant, California, USA).

Energy-dispersive x-ray spectroscopy (EDS) was carried out using the Oxford Link system attached to the TEM.

Room-temperature optical spectra in the ultraviolet and visible light wavelength ranges were collected using a CARY 5000 spectrophotometer fitted with an integrating sphere diffuse reflectance accessory. The spectrophotometer measures reflectance relative to a background scatterer, which was powdered $BaSO_4$.

X-ray photoelectron spectroscopy (XPS) measurements were performed using a Physical Electronics Quantum 2000 scanning ESCA microprobe. This system uses a focused monochromatic Al Kα x-ray (1486.7 eV) source and a spherical section analyser. The instrument has a 16-element multichannel detector. The x-ray beam used was a 105 W, 100 μm diameter beam that was rastered over a 1.4 mm by 0.2 mm rectangle on the sample. The x-ray beam was incident normal to the sample and the photoelectron detector was at 45° off-normal. Data were collected using a pass energy of 46.95 eV. For the Ag $3d_{5/2}$ line, these conditions produce a full width at half maximum (FWHM) of better than 0.98 eV. Although the binding energy (BE) scale was calibrated using the Cu $2p_{3/2}$ feature at 932.62 ± 0.05 eV and the Au 4f feature at 83.96 ± 0.05 eV for known standards, the Co-doped ZnO surface experienced variable degrees of charging. Low-energy electrons at $\sim$1 eV, 21 μA and low-energy Ar$^+$ ions were used to minimize this charging. The BE positions were referenced using a 530.4 eV position for the O 1s feature.

Magnetic measurements were carried out as a function of temperature (4–350 K) and magnetic field (0 to $\pm$65 kOe) using a commercial magnetometer (Quantum Design, PPMS) equipped with a superconducting magnet. Measurements were carried out on tightly packed powder samples placed in a clear plastic drinking straw. The data reported here were corrected for the background signal from the sample holder (clear plastic drinking straw) with diamagnetic susceptibility $\chi = -4.1 \times 10^{-8}$ emu Oe^{-1}. Data analyses were carried out using Mathsoft's Mathcad. High-temperature magnetic measurements were carried out using a vibrating sample magnetometer equipped with a high-temperature (300–1000 K) oven.

3. Experimental results and analysis

3.1. Particle-induced x-ray emission (PIXE) studies

PIXE measurements were employed to estimate the Co concentrations of the $Zn_{1-x}Co_xO$ samples. The PIXE data along with its theoretical fit showing the Co and Zn regions obtained from a representative sample with $x = 0.02$ are shown in figure 1. The Co concentrations, estimated by simulating the experimental PIXE spectra after removing the background due to bremsstrahlung, are listed in table 1.

3.2. X-ray diffraction studies

The undoped ZnO and the $Zn_{1-x}Co_xO$ nanoparticles prepared by annealing the reaction precipitate at 350 °C showed a well-defined wurtzite structure. The XRD patterns of the $Zn_{1-x}Co_xO$ samples did not show any peaks other than that of ZnO for $0 \leqslant x \leqslant 0.12$ (figure 2(a)). The samples prepared under identical conditions but with no Zn precursor ($x = 1$) showed Co_3O_4 peaks only, suggesting that any unincorporated Co will most likely form Co_3O_4. Since the detection limit of the XRD system employed was $\sim$2%, this indicates that most of the dopants, if not all, are incorporated into the host ZnO lattice. The peak intensities, positions and widths of the XRD lines changed with x in $Zn_{1-x}Co_xO$, as illustrated in figures 2(a) and (b). The peaks shifted to higher angles as x increased to 0.03, above which the peaks showed a large shift to the low angle side followed by moderate changes, as illustrated in figure 2(b).
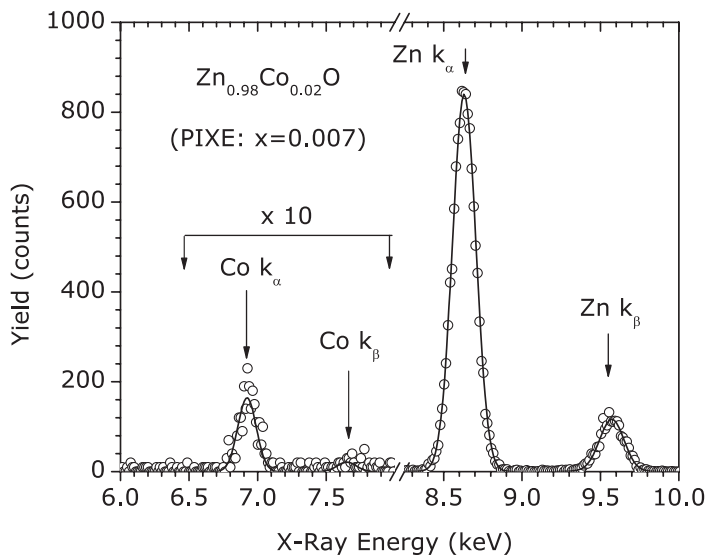
Figure 1. Typical PIXE spectra from the $Zn_{0.98}Co_{0.02}O$ sample showing the Co and Zn regions. Co concentrations (x) obtained by PIXE data simulation (solid line) are given in parentheses.

Table 1. Atomic concentration estimates of $Zn_{1-x}Co_xO$ obtained from PIXE and XPS measurements.

Nominal Co%	Estimated Co atomic% from PIXE	Preparation temperature (°C)	Processing conditions	Estimated atomic% from XPS			
				Co	Zn	O	O/(Zn + Co)
0	—	350	As-prepared	0.0	53.3	43.3	0.8
2	0.7	350	As-prepared	1.1	49.5	45.4	0.9
3	1.7	350	As-prepared	5.4	44.5	44.9	0.9
8	7.3	350	As-prepared	—	—	—	—
12	10.8	350	As-prepared	5.9	38.9	47.6	1.1
12	—	350	As-prepared	5.9	38.9	47.6	1.1
12	—	350	10 nm Ar+ ion sputtered	7.4	46.2	44.2	0.8
12	—	350	20 nm Ar+ ion sputtered	7.5	47.0	43.9	0.8

These changes are very similar to those observed by others [36, 43] in $Zn_{1-x}Co_xO$ thin films prepared by pulsed laser ablation and in $Sn_{1-x}Co_xO_2$ powders by the authors [44]. Changes in the lattice parameters a and c, estimated using the hexagonal (102) and (110) peaks of the nanoscale samples of $Zn_{1-x}Co_xO$, are shown in figure 3(a). The a and c parameters of the undoped ZnO powder are slightly lower than those reported for bulk ZnO probably due to the smaller size of the particles and/or changes in the oxygen stoichiometry. Clearly, the ZnO lattice contracts as x increases to 0.03. This may be due to the substitutional doping of Co^{2+} in tetrahedral Zn^{2+} lattice sites. The ionic size of high-spin tetrahedral Co^{2+} is 0.58 Å, which is smaller than the 0.60 Å sized Zn^{2+} [45]. Above $x = 0.03$, the observed increase in the lattice parameters (figure 3(a)) suggests additional interstitial incorporation of Co^{2+} similar to that observed in Co-doped SnO_2 [44] or additional incorporation of Co^{3+} ions with significant lattice defects [43]. The latter possibility is ruled out due to the lack of any indication of Co^{3+} states in the XPS data of the 12% Co-doped samples presented elsewhere in this paper. The increased coordination number for the Co^{2+} in interstitial sites results in a larger ionic radius [36, 44, 45]. Both low-spin and high-spin Co^{2+} ions in octahedral coordination have

5
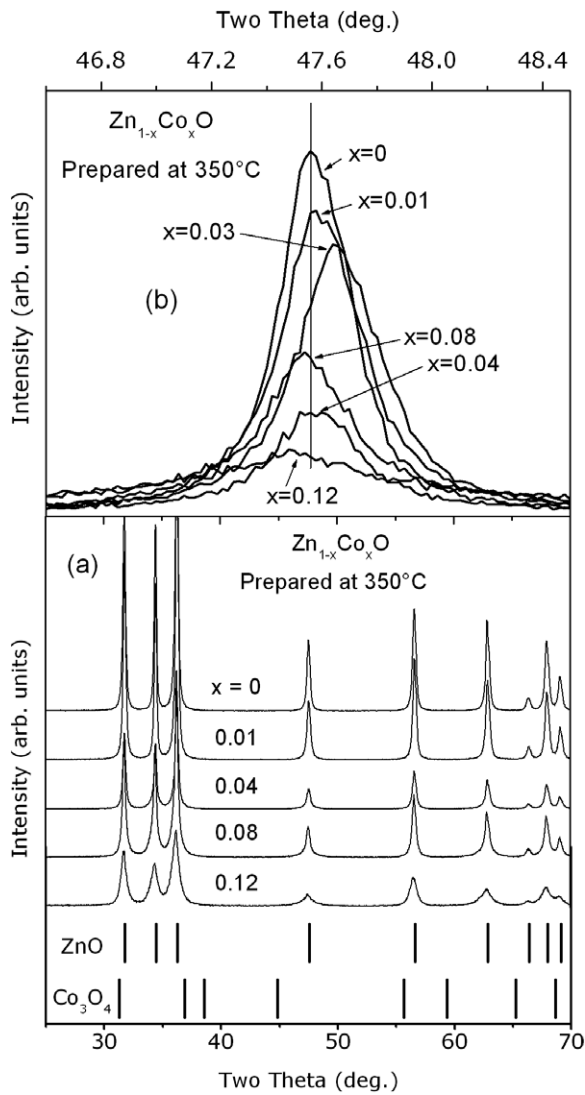
Figure 2. Panel (a) shows XRD patterns of the $Zn_{1-x}Co_xO$ samples along with reference lines of wurtzite ZnO and Co_3O_4. Panel (b) illustrates the changes in the peak widths and peak positions with increasing x. The lines indicate the reference data of ZnO and Co_3O_4.

larger ionic radii of 0.65 and 0.745 Å respectively, which can well explain the increase in the lattice parameters [45]. The particle size L of the samples were calculated using the (100), (103) and (110) peaks and using the Scherrer relation, $L = \frac{0.9\lambda}{B\cos\theta}$ (where θ is the peak position, λ is the x-ray wavelength and $B = (B_m^2 - B_s^2)^{1/2}$ was estimated using the measured peak width B_m and the instrumental width B_s). With increasing x, the particle size gradually decreases and shows rapid changes for $x > 0.06$, as illustrated in figure 3(b). This suggests that Co incorporation into the ZnO lattice decreases the grain growth, as observed in other systems also [44, 46].

3.3. Transmission electron microscopy studies

TEM measurements showed drastic changes in the shape and size of the $Zn_{1-x}Co_xO$ particles with different Co doping concentrations, as illustrated in figure 4. For the undoped ZnO and the
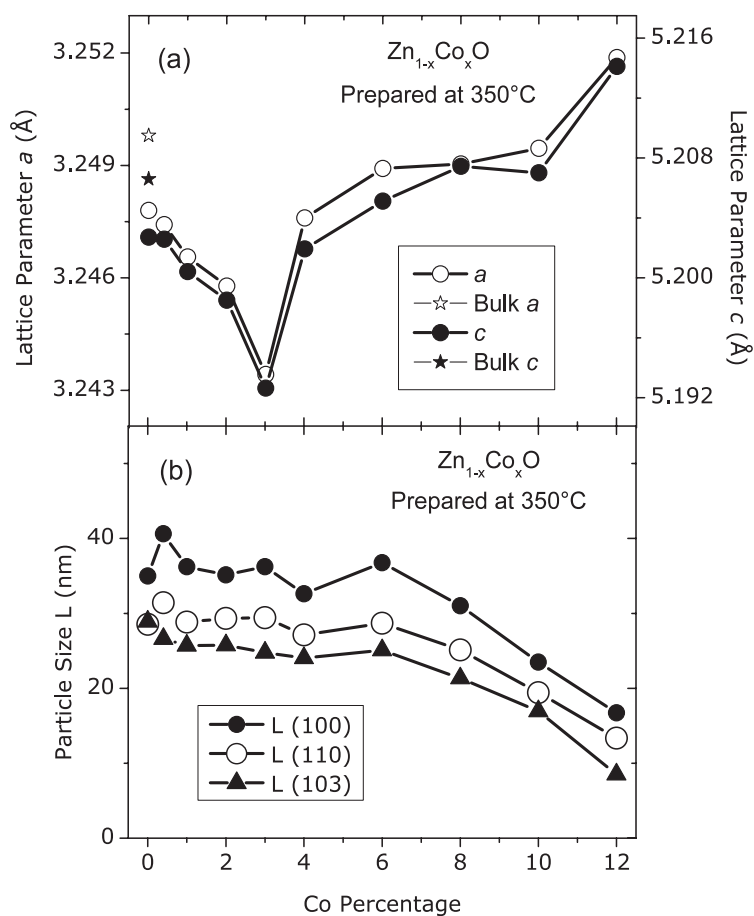
Figure 3. Panel (a) shows changes in the lattice parameters *a* and *c* of hexagonal ZnO calculated using the (102) and (110) peaks as a function of Co percentage; stars indicate the *a* and *c* parameters reported for bulk ZnO; panel (b) shows the particle size of $Zn_{1-x}Co_xO$ samples as a function of *x* calculated using the (100), (110) and (103) XRD peaks.

$Zn_{1-x}Co_xO$ particles with $x < 0.06$, the hexagonal-shaped particles were all elongated with their lengths and widths in the 90–120 and 40–80 nm range respectively, giving aspect ratios in the 1.25–2.0 range. For $x > 0.06$, there is a dramatic change in the particle size and shape, with $L < 10$ nm (figures 4(e) and (f)). The reduction in the crystallite size with increasing *x* observed in the TEM images agrees reasonably well with the estimates obtained from the XRD data shown in figure 3(b).

The electron diffraction patterns (EDPs) obtained from the samples further confirmed the wurtzite phase of ZnO (shown as insets in figure 4). The EDP data were collected from samples with different *x* and provided no evidence of any impurity phases for $x \leqslant 0.12$. The EDP data were taken from multiple spots within the same sample, confirming the phase purity and the absence of impurity clusters of Co or its oxides throughout. EDS measurements showed an increase in the relative intensities of the Co peaks with increasing *x*, confirming the progressive incorporation of Co. The EDS measurements (figure 5) were carried out at different regions of the same sample showing comparable Co concentrations. This ensures the uniform distribution of the doped Co ions as expected in the chemical synthesis process employed in this work.
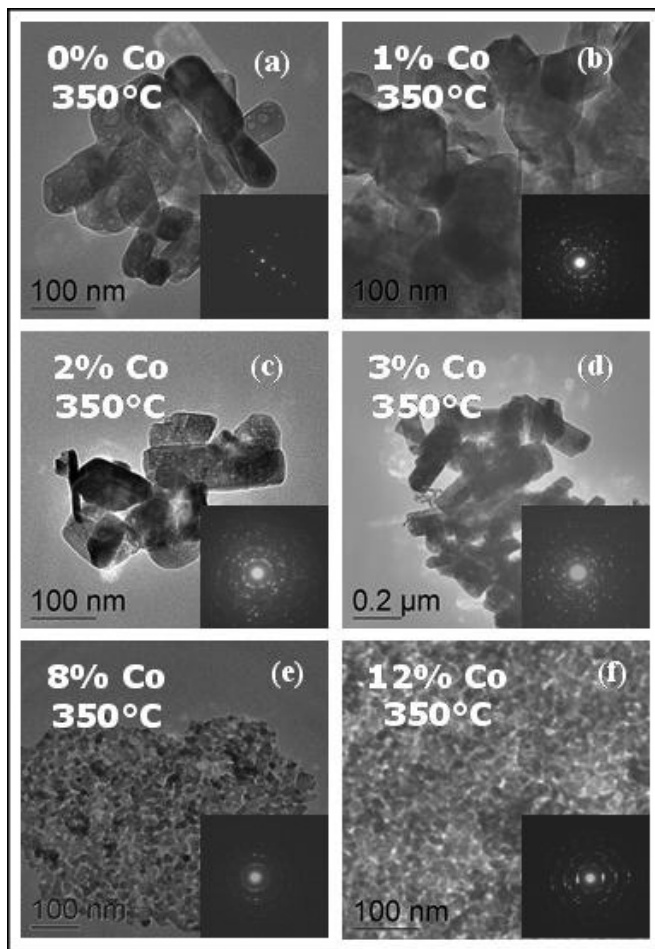
Figure 4. Panels (a)–(f) show TEM images of $Zn_{1-x}Co_xO$ samples with $x = 0$, 0.01, 0.02, 0.03, 0.08 and 0.12 respectively. The inset in each panel shows an electron diffraction pattern taken from the sample.

3.4. Raman spectroscopy studies

Representative Raman spectra taken from the $Zn_{1-x}Co_xO$ powder samples are shown in figure 6(a). These data have been vertically adjusted for clarity and are enhanced by the factors shown. Two Raman peaks occur near 330 and 437 cm^{-1} in ZnO [47, 48]. The peak near 330 cm^{-1} is often attributed to multiple phonon processes; however, a detailed assignment has not been agreed upon, while the peak at 437 cm^{-1} is assigned to the E_2 phonon mode. The top curve in figure 6(a) is from the undoped powder sample which had an intense broad PL emission band underlying the region of these Raman modes when excited using 514.5 nm light. The background PL intensity from this sample has been subtracted from the raw data in order to obtain these data for the undoped powder.

As the cobalt composition in the powder samples increased, the Raman intensity decreased. For $x \geqslant 0.04$, the E_2 mode near 437 cm^{-1} was broadened and the peak had shifted slightly, as shown in figure 6(b). This is the same region where XRD data show an expansion of the lattice, indicating interstitial incorporation of Co. This interstitial incorporation of Co might have caused significant structural disorder in ZnO, producing the observed changes in the line width and position of the Raman peaks. Similar changes in Raman data have been reported for Co-doped SnO_2 powders [44]. The most probable impurity phase, Co_3O_4, has major peaks at

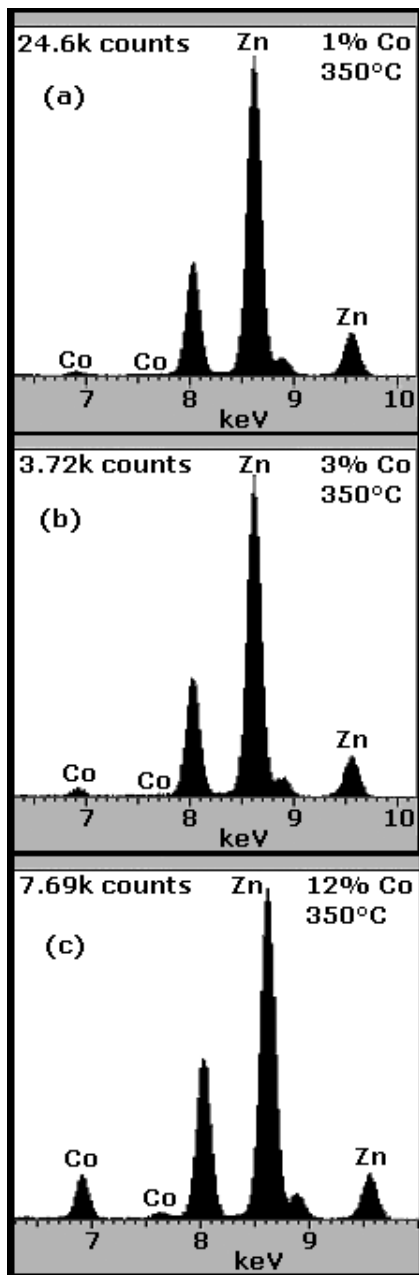**Figure 5.** Panels (a)–(c) show EDX data of $Zn_{1-x}Co_xO$ samples with $x = 0.01$, 0.03, and 0.12 respectively.

196, 480, 520, 617 and 688 cm^{-1} [49, 50]. The absence of these peaks in the Raman data of $Zn_{1-x}Co_xO$ shows that they are free from this most probable impurity phase.

3.5. Optical spectroscopy measurements

Optical characterization of the pure and Co-doped ZnO powders in the UV and visible energy ranges were carried out by measuring the diffuse reflectance at room temperature. Figure 7(a)
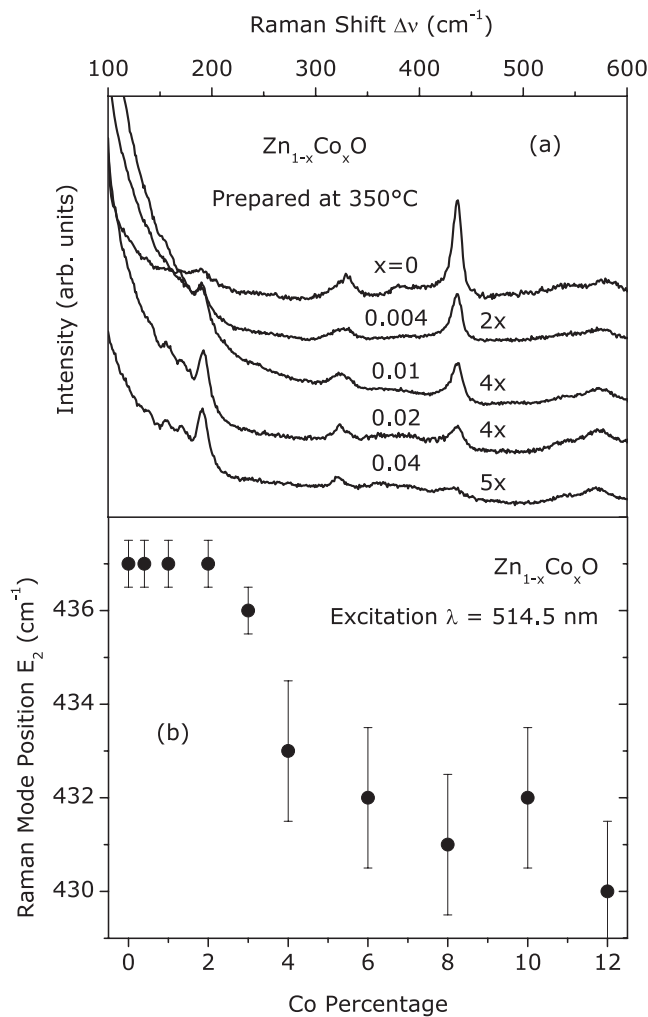
Figure 6. Panel (a) shows the room-temperature Raman spectra of several $Zn_{1-x}Co_xO$ samples. Panel (b) illustrates the changes in the E_2 mode (437 cm^{-1}) position.

shows the room-temperature spectra indicating three well-defined absorption edges at 660, 615 and 568 nm, respectively. Based on the optical studies of Co-doped ZnO single crystals by Weakliem [51], these edges are assigned to the d–d crystal-field transitions $^4A_2(F) \rightarrow {}^2E(G)$, $^4A_2(F) \rightarrow {}^4T_1(P)$ and $^4A_2(F) \rightarrow {}^2T_1(G)$. The appearance of these transitions clearly suggests that the doped Co^{2+} is in the high-spin ($S = 3/2$) state and are under a tetrahedral crystal field, in agreement with similar studies on $Zn_{1-x}Co_xO$ thin films [39, 43]. Wurtzite ZnO has Zn^{2+} ions in tetrahedral sites [36] and therefore Co^{2+} ions seem to substitute for the Zn^{2+} ions in the ZnO lattice. It may be noted that the relative intensity of the absorption edges at 660, 615 and 568 nm, shown in figure 7(b), saturates for $x > 0.03$, indicating that any additional Co ions incorporated into the ZnO lattice may be occupying sites with a different local crystal field. This is in agreement with the changes in the lattice parameters estimated from the XRD data in which interstitial incorporation of Co ions is indicated for $x > 0.03$.

The diffuse reflectance of the sample is related to the Kubelka–Munk function $F(R)$ by the relation $F(R) = (1 - R)^2/2R$, where R is the percentage reflectance [52]. The direct band gap (E_g) energies of the $Zn_{1-x}Co_xO$ powders were calculated from their diffuse-reflectance
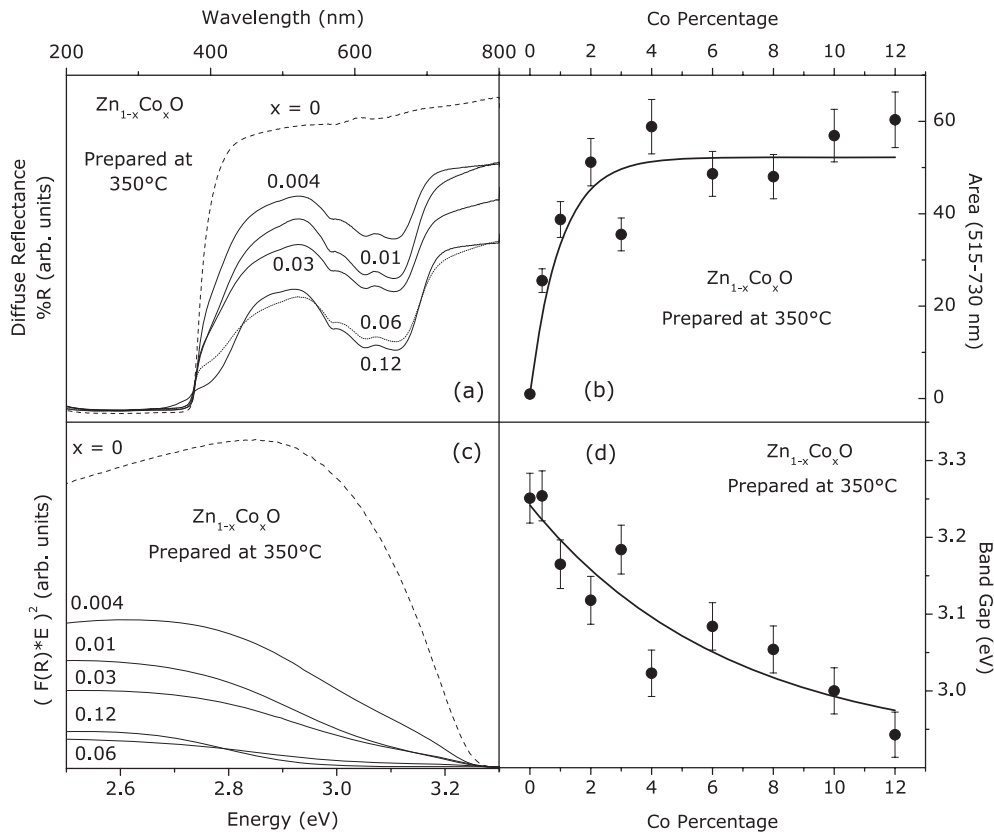
Figure 7. Panel (a) shows the room-temperature diffuse reflectance spectra of $Zn_{1-x}Co_xO$ samples. Panel (b) shows the variation of the area under the absorption bands (in panel (a)) with x. Panel (c) shows $[F(R) * E]^2$ versus energy and (d) shows the variation of the band gap energy with x. The trend lines through the data points in (b) and (d) are a visual aid.

spectra by plotting $[F(R) \times E]^2$ versus energy E in electron volts. The linear part of the curve was extrapolated to $[F(R) \times E]^2 = 0$ to estimate the direct band gap energy shown in figure 7(c). The band gap of the Co-doped ZnO samples decreases with increasing x, as shown in figure 7(d). A similar decrease in the band gap energy with Co concentration has recently been reported in Co-doped ZnO thin films by Kim and Park [43], although an opposite behaviour was observed by Schwartz *et al* [49] in $Zn_{1-x}Co_xO$ nanocrystals. Kim and Park [43] have argued that the band gap narrowing with increasing x is due to the *sp–d* exchange interactions between the band electrons and the localized *d* electrons of the substituted Co^{2+} ions. Ando *et al* [22] have reported a large magneto-optical effect in $Zn_{1-x}Co_xO$—the largest observed among the various transition metal dopants employed—indicating strong exchange interaction between the *sp* band electrons and the localized *d* electrons, thus supporting this possibility.

3.6. Photoluminescence spectroscopy measurements

The PL spectra collected at room temperature from $Zn_{1-x}Co_xO$ samples with varying x are shown in figure 8(a). At 300 K, these samples exhibit two emission bands, one peaking near
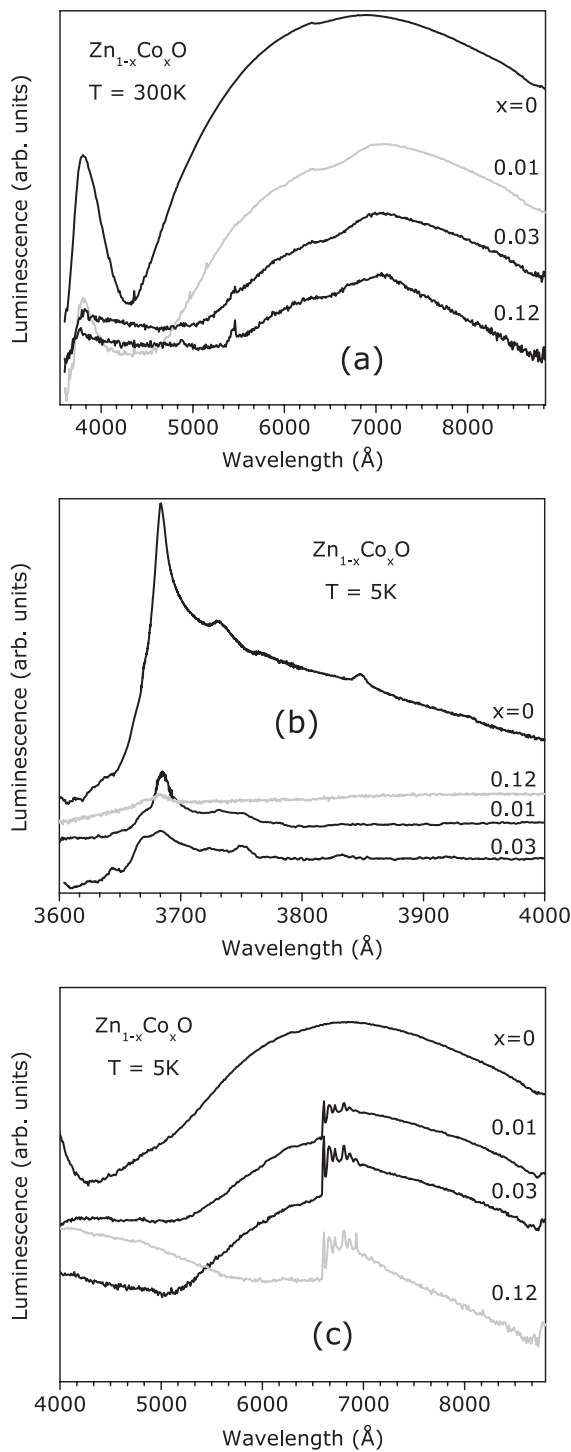
Figure 8. Photoluminescence data taken at (a) 300 K, (b) 5 K (edge-emission region), and (c) 5 K (deep-level region) from representative $Zn_{1-x}Co_xO$ samples. The structured emission in (c) corresponds to localized d–d transitions of isolated Co^{2+} ions. The excitation power density was $1\,W\,cm^{-2}$.

380 nm attributed to the superposition of free-exciton and phonon-sideband emissions [53], and one broad visible band peaking near 685 nm. This very bright visible emission from

the $x = 0$ sample was also produced by the 514.5 nm below-band-gap excitation used for the Raman measurements. The emission involves some unidentified deep levels, and is not associated with the cobalt. With increasing cobalt concentration, the PL intensity is quenched. At 300 K, the reduction in the emission intensity from about 600 to 660 nm is due to the competing superposition of the $^4A_2(F) \rightarrow {}^2E(G)$ and $^4A_2(F) \rightarrow {}^4T_1(P)$ and $^4A_2(F) \rightarrow {}^2T_1(G)$ absorptions due to isolated Co^{2+} ions in the ZnO lattice [51]. The $x = 0$ sample shows a small decrease in the PL intensity in this range. As shown in figure 8, EPR detected a signal due to a small amount of Co^{2+} ions in the $x = 0$ sample due to unintentional doping. The edge emission peak at 300 K did not exhibit any clear shifts due to cobalt doping, even for $x = 0.12$, which differs from the reflectance measurements discussed above. The reflectance measurements may be more sensitive to the near-surface regions of the powders. This might suggest that the effective doping concentrations and processes may be different between the core and surface regions of the $Zn_{1-x}Co_xO$ particles.

At 5 K, the edge emission from the undoped powder is dominated by a bound exciton peaking near 368 nm, in good agreement with crystalline ZnO. With increasing cobalt doping, the edge emission is quenched. At low temperature, the deep-level emission from the $x = 0$ sample is very intense. The Co^{2+}-related absorption in the visible produces the decrease in the broad PL band out to about 660 nm. The structured PL emission at wavelengths just beyond 660 nm are transitions from the mixed $^4T_1(P)$, $^2T_1(G)$, $^2E(G)$ levels to the $^4A_2(F)$ ground state of the isolated Co^{2+} ions on zinc sites [54]. Even for $x = 0.12$, the PL emission due to Co^{2+} proves there is some fraction of the cobalt ions incorporated substitutionally in the ZnO host and in an unperturbed environment.

3.7. X-ray photoelectron spectroscopy studies

The high-resolution XPS spectra of pure ZnO, 2% and 12% Co-doped ZnO and a Co_3O_4 sample (prepared under identical conditions but with no Zn precursor) were taken to investigate the electronic state and chemical environment of the Co ions incorporated in the ZnO lattice. Figure 9 shows the Co core-level region of the XPS spectra measured at room temperature from these samples. Comparing the binding energies of the Co primary and satellite XPS peaks with those observed for $Co(0)$ in Co metal, Co^{2+} in CoO and Co^{3+} in γ-Co_2O_3 [55, 56], the electronic state of the Co in the measured samples is found to be Co^{2+} and that it is not bonded to oxygen as CoO or Co_3O_4. The binding energies obtained also rule out any metallic Co clusters in the samples. These results agree well with the 2+ oxidation state of Co with $S = 3/2$ determined from EPR, optical and magnetization measurements discussed elsewhere in this paper. The $\geqslant 1.3$ eV shift of the Co $2p_{3/2}$ peak in the $Zn_{1-x}Co_xO$ samples relative to this peak in the Co_3O_4 reference sample suggests that Co is indeed incorporated in the ZnO lattice and does not form any measurable amount of this most probable impurity oxide. Also, no significant change in the Co binding energy is observed with increasing Co doping concentration. Careful analysis of the Zn $2p_{3/2}$ (1021.7 eV) peak positions also did not show any noticeable change in the binding energy with increasing Co concentration. Atomic percentages of Zn, Co and O calculated using the Zn $3d_{3/2}$ (1021.7 eV), O 1s (530.65 eV), and Co $2p_{3/2}$ (781.1 eV) are shown in table 1. As the Co concentration increases, the Zn concentration decreases, suggesting that at least a fraction of the doped Co ions are substitutionally replacing Zn ions for the entire range of $0 < x \leqslant 0.12$, in agreement with similar results from the XRD and optical data.

In a recent report, Schwartz *et al* [49] have shown that the doped Co ions have an increased tendency to occupy the surface sites of the nanoscale $Zn_{1-x}Co_xO$ particles when prepared using chemical methods at low temperatures. Similar effects of transition metal ion diffusion to the particle surface causing a non-uniform distribution of the dopant atoms within the individual
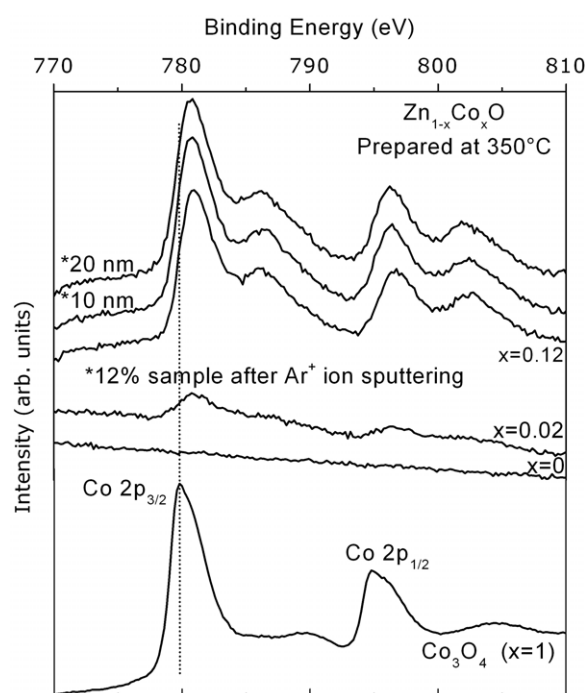
Figure 9. XPS spectra of $Zn_{1-x}Co_xO$ samples with different values of x as indicated. Reference data obtained from Co_3O_4 prepared under identical synthesis conditions (but with no Zn precursors) are also shown. The top two data curves are obtained from the sample with $x = 0.12$ after removing 10 and 20 nm of surface layers.

particles have been reported by the authors in other semiconductor oxide systems recently [57]. Since XPS is a surface-sensitive technique, the authors [57] have shown recently that collecting XPS data after progressive removal of surface layers by Ar ion sputtering could verify this possibility. We investigated this possibility by collecting the XPS spectra of the $Zn_{0.88}Co_{0.12}O$ samples after removing two consecutive layers of 10 nm each from the surface after attaching the particles to carbon conductive tape. As shown in table 1, the XPS data provided no evidence of increased Co incorporation on the particle surface, suggesting that the doped Co ions are distributed throughout the particle. However, with increasing Co doping level, the oxygen content—given by the estimated atomic percentage ratio $[O/(Zn + Co)]$ from XPS—decreases systematically from 0.8 in undoped ZnO to as high as 1.1 in the $Zn_{0.88}Co_{0.12}O$ sample. This suggests that compared to the oxygen-deficient undoped ZnO and the other samples with $x < 0.12$, the 12% Co-doped samples has excess oxygen. This is an important difference since the n-type semiconducting behaviour of oxides results from the oxygen deficiency. The XPS data collected from the $Zn_{0.88}Co_{0.12}O$ sample before and after the Ar ion sputtering (see table 1) show that the surface region contains more than stoichiometric oxygen concentration. The surface region also showed a lower Zn concentration, probably indicating the presence of some Zn vacancies. Interestingly, both excess oxygen and the presence of Zn vacancies in ZnO are favourable factors to produce p-type conduction [30]. However, the inner (core) regions of the particles investigated after removing the surface layers by sputtering were oxygen deficient and had a higher Zn concentration.

Interstitial Co^{2+} incorporation would require additional oxygen ions and/or Zn vacancies for charge neutrality. Since such excess oxygen ions are easier to attain in the near-surface region of the particles, it may be likely to have relatively more interstitial incorporation of Co ions in the surface region compared to the core of the particles. This would suggest that, with increasing Co doping, a larger surface-to-volume ratio is required due to the increased

interstitial incorporation of Co in the samples. From XRD, diffuse reflectance and Raman studies, it was observed earlier that substitutional doping saturates for $x \sim 0.03$, and above this level Co enters in interstitial sites. This leads to the gradual reduction in the particles size when $x > 0.03$ observed in XRD (figure 3(b)) and TEM (figure 4) data.

### 3.8. Electron paramagnetic resonance spectroscopy studies

Figures 10(a) and (b) show the EPR spectra of the 2 and 12% Co-doped ZnO samples. The cobalt atoms substitute for the zinc atoms, thus the neutral charge state is Co^{2+} (a $3d^7$ configuration). The EPR parameters for an isolated Co^{2+} in ZnO have been reported [58]. Co^{59} has $I = 7/2$ (100% abundant) which gives rise to an eight-line pattern in single crystals when the magnetic field is along the c-axis in single crystals. The effective g values are about 2.2 and 4.5 for $H \perp c$ and $H \parallel c$, respectively. For the $Zn_{1-x}Co_xO$ powder samples, the EPR data represent an averaged spectrum over all field orientations. The signals near 1500 and 3000 G correspond to the effective $g_\perp$ and $g_\parallel$, respectively. For low x values, the spectrum is dominated by a sharp peak at $g \sim 4.5$ (see figure 10(a)). Several samples also had much weaker EPR signals due to substitutional Mn^{2+} centred near 3300 G (i.e., near $g = 2$), and also a weak single-line signal near $g = 1.96$, most likely due to shallow donors [59]. The spectrum from the $x = 0.12$ sample shown in figure 10(b) is enhanced by a factor of 5, and the weak $g = 1.96$ signal can be observed. For $x > 0.04$, the 1500 G signal became increasingly broadened and changed in lineshape until the result shown in figure 10(b). The isolated Co^{2+} sharper line is still apparent, but a large concentration of spins is contributing to the much broader ($\sim$ several hundreds of gauss in linewidth) superimposed signal. A similar broadening behaviour was observed in a (Zn, Co)O thin epitaxial film for a nominal 10% Co concentration [58].

Figure 10(c) shows the relative changes in the signal intensity of these two superimposed EPR spectra as a function of x. The double integration of the EPR spectrum was used to obtain a relative signal from each sample. These 'area' values have been normalized to the value obtained from the $x = 0.04$ sample. The spin concentration related to the EPR spectrum increases with cobalt doping only up to $x = 0.04$; however, not at the rate expected if all cobalt ions were contributing to the EPR signal. Above this critical doping value, the integrated area saturates. This supports the results from the XRD, diffuse reflectance and Raman spectroscopy experiments, which suggest some non-substitutional incorporation of Co for $x > 0.03$. The broad spectrum in these powder samples is most likely caused by the magnetic interactions between close-lying Co^{2+} ions, i.e., Co^{2+} at the next-nearest neighbour or slightly more distant cation sites. However, if Co–Co pairs were formed at the higher doping concentrations (as may occur with interstitial formation), those cobalt ions would not be expected to contribute to the EPR signal representing isolated impurities.

The spectrum in figure 10(b) for the $x = 0.12$ powder sample still shows the sharper EPR-line signal due to unperturbed Co^{2+} ions, in addition to the broader signal. These data suggest that there exists a non-uniform incorporation of the cobalt impurities within the ZnO particles or there exist different types of magnetic interactions between the doped Co^{2+} ions in different regions within the individual particles.

3.9. Magnetic measurements

M versus H plots of $Zn_{1-x}Co_xO$ samples with $x \leqslant 0.10$ measured at 300 K showed a linear variation owing to the paramagnetic behaviour, as shown in figure 11(a). However, the 12% Co-doped sample showed a saturating component in addition to the linear paramagnetic component. If this linear component at high fields $\chi_p = 8.22 \times 10^{-6}$ emu g^{-1} Oe^{-1} is subtracted, the $M - \chi_p H$ data show the saturation of M expected for a ferromagnetic
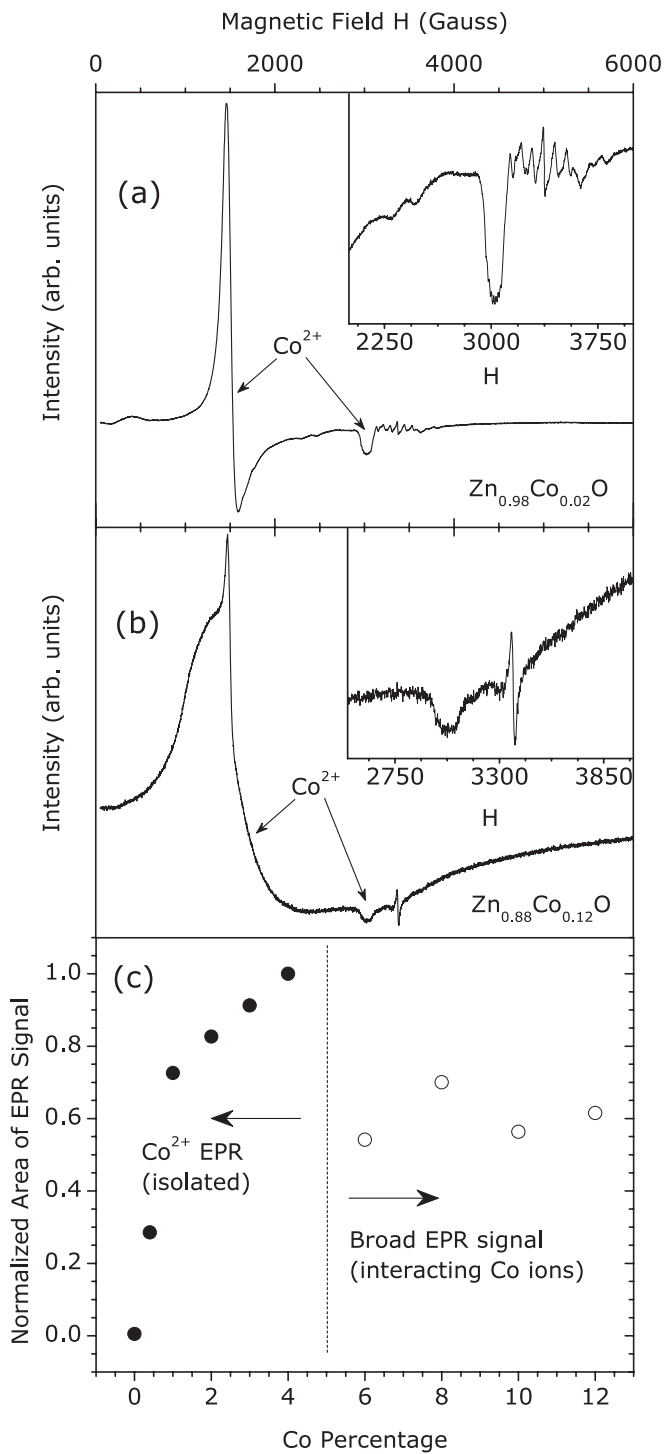
Figure 10. Panels (a) and (b) show EPR spectra of $Zn_{1-x}Co_xO$ samples with $x = 0.02$ and 0.12 respectively. The insets in (a) and (b) show expanded views of the $g \sim 2$ region. Panel (c) shows the variation of the EPR integrated area of the two different EPR signals with x.

phase (figure 11(b)). The data collected at 5 K from the $Zn_{1-x}Co_xO$ samples also showed a paramagnetic-like component, thus enabling the data to be described with the modified

16
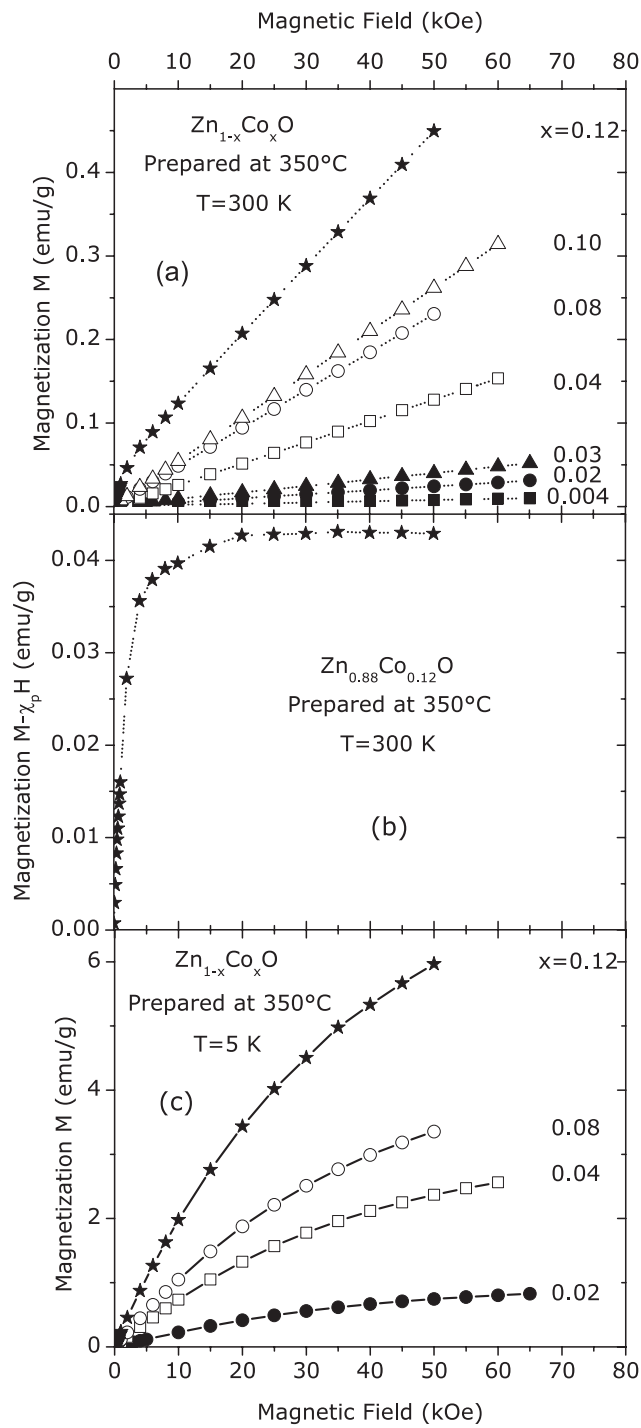
Figure 11. Panel (a) shows *M* versus *H* data of selected $Zn_{1-x}Co_xO$ samples measured at 300 K. Panel (b) is a plot of the $M-\chi_p H$ versus *H* showing the saturating magnetic behaviour expected for a ferromagnetic phase for the 12% Co-doped ZnO sample. Panel (c) shows *M* versus *H* data of selected $Zn_{1-x}Co_xO$ samples measured at 5 K. Solid lines through the data points are theoretical fits using equation (1).
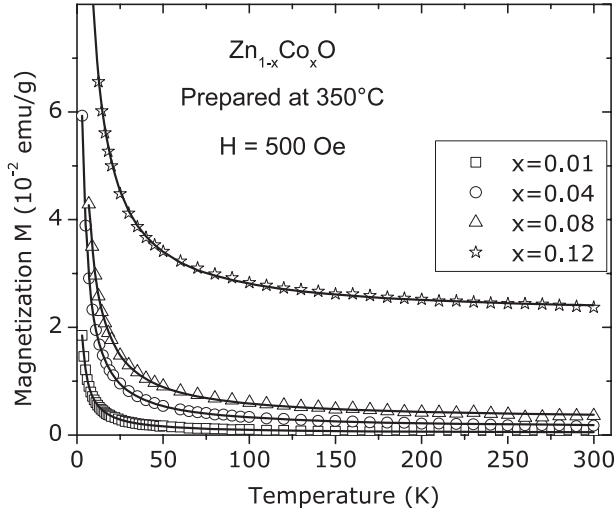
Figure 12. *M* versus *T* data measured with *H* = 500 Oe from selected $Zn_{1-x}Co_xO$ samples. Solid lines are theoretical fits using the modified Curie–Weiss law.

Brillouin function [57, 60]. This indicates that all of the Co ions present in $Zn_{1-x}Co_xO$ with $x \leqslant 0.10$ and a significant fraction of the doped Co in the $Zn_{0.88}Co_{0.12}O$ sample are paramagnetic. In figure 11(c), the magnetization *M* of selected $Zn_{1-x}Co_xO$ samples as a function of magnetic field *H* measured at 5 K is shown along with their theoretical estimates obtained using the modified Brillouin-function-based form [57, 60] for a paramagnetic system, given by

$$M = M_0 \left\{ \left(\frac{2J+1}{2J} \right) \coth \left[\frac{(2J+1)y}{2J} \right] - \left(\frac{1}{2J} \right) \coth \left(\frac{y}{2J} \right) \right\} \tag{1}$$

where $y = \frac{g\mu_B J H}{kT}$, M_0 is the saturation magnetization, $g = 2.0023$ is the spectroscopic splitting factor for free electrons [61], μ_B is the Bohr magneton and k is the Boltzmann constant. Based on the EPR, optical and XPS data discussed before, this analysis was carried out by assuming $J = 3/2$, as expected for high-spin Co^{2+}.

The magnetization *M* of the $Zn_{1-x}Co_xO$ samples measured as a function of temperature *T* at a constant applied field $H = 500$ Oe, shown in figure 12, also demonstrated a clear paramagnetic behaviour. The data were fitted using the modified Curie–Weiss law $\chi = \chi_0 + \frac{C}{T+\theta}$, where χ_0 represents non-paramagnetic contributions [57, 62], the Curie constant $C = N\mu^2/3k$ (N = number of magnetic ions/g, μ = magnetic moment of the ion) and θ is the Curie–Weiss temperature. The feeble values of $\chi_0 = 2.5(2) \times 10^{-6}$ emu g^{-1} Oe^{-1} for $Zn_{1-x}Co_xO$ samples with $x \leqslant 0.10$ indicate that there are no significant non-paramagnetic phases in these samples. However, for $x = 0.12$, $\chi_0 = 45 \times 10^{-6}$ emu g^{-1} Oe^{-1} clearly indicates the presence of a non-paramagnetic phase. Based on the *M* versus *H* behaviour observed in figure 11(a), this must be the FM component that has developed in the sample. These fits showed a gradual increase in *C* and M_0 with x, as shown in figure 13(a), confirming the progressive doping of Co ions in ZnO since both *C* and M_0 are direct functions of N, the number of Co^{2+} spins. The positive values of θ indicate AF interactions between the Co spins as also observed in other systems [57]. θ increases with x, indicating that the AF interaction between the paramagnetic spins increases with increasing Co doping (see figure 13(b)).

The ferromagnetic $Zn_{0.88}Co_{0.12}O$ samples showed a well-defined hysteresis loop at 300 K (figure 14) with a coercivity $H_c \sim 350$ Oe, remanence $M_r \sim 25\%$ and saturation magnetization $M_s \sim 0.04$ emu g^{-1}. This low value of M_s and the strong presence of the paramagnetic
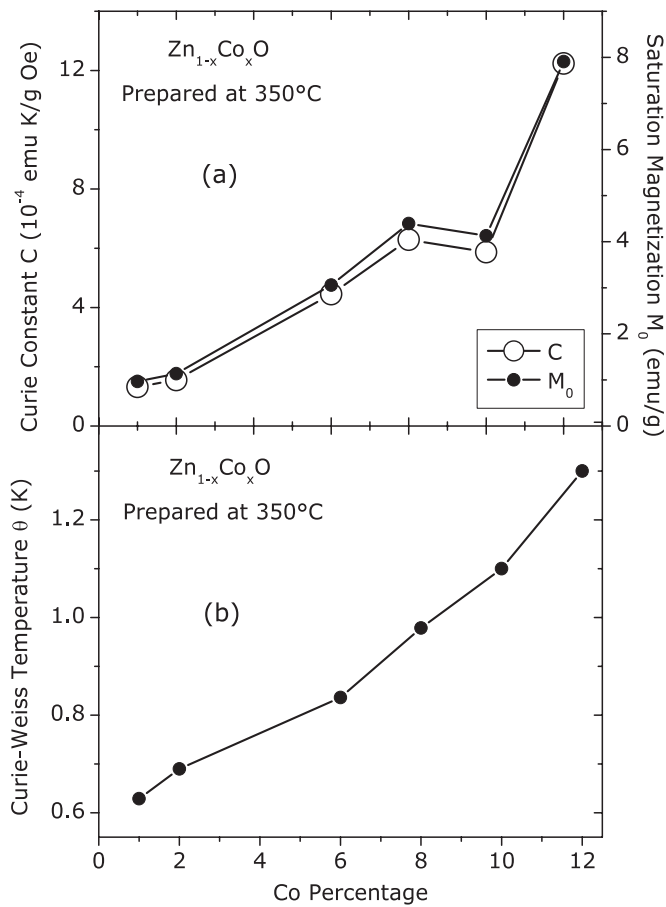
Figure 13. Panel (a) shows changes in the saturation magnetization M_0 and Curie constant C of the $Zn_{1-x}Co_xO$ samples as a function of x. Panel (b) shows changes in the Curie–Weiss temperature θ of the $Zn_{1-x}Co_xO$ samples as a function of x. θ and C were obtained from the data in figure 12. M_0 was obtained from the data in figure 11(c).
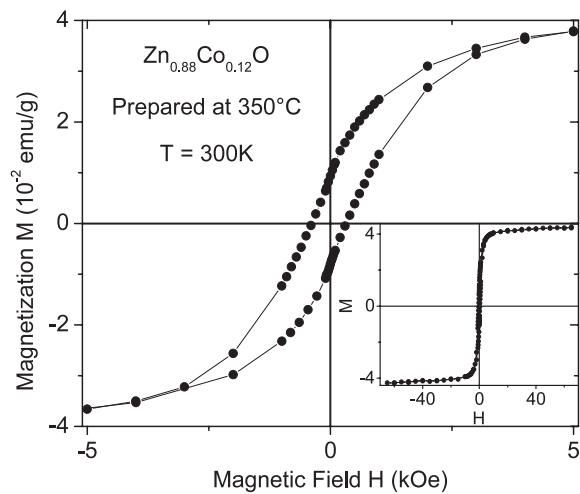
Figure 14. Room-temperature hysteresis loop taken on $Zn_{0.88}Co_{0.12}O$. The inset shows the loop over the entire magnetic field range employed. The lines joining the points are a visual aid.

component observed in this sample suggest that only a small fraction of the doped Co^{2+} ions participate in the ferromagnetically coupled state. The loop, however, also displayed a small negative shift of ∼30 Oe at 300 K. In several magnetic systems, such a shift of the hysteresis
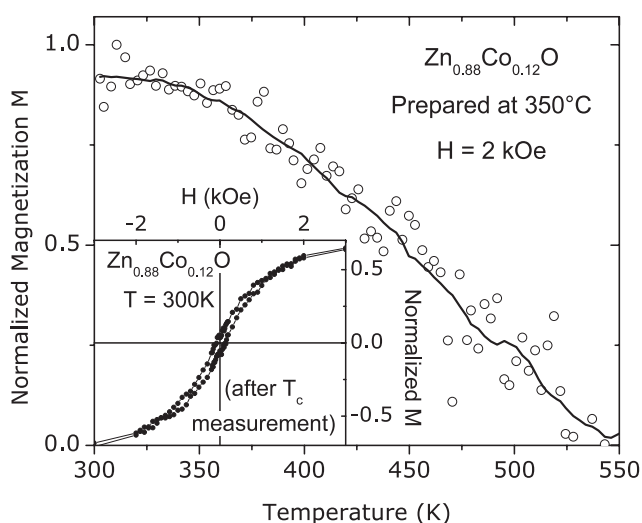
Figure 15. Plot of the normalized sample magnetization of a $Zn_{0.88}Co_{0.12}O$ sample (measured with $H = 2$ kOe) as a function of temperature, indicating a Curie temperature $T_c \sim 540$ K. The inset shows the hysteresis loop obtained upon returning to room temperature after the T_c measurement.

loop is associated with a phenomenon known as exchange bias [63–65], and is observed due to FM–AF interfaces. Since all the known Co oxides are paramagnetic at or above room temperature, the existence of such an exchange bias at 300 K and above clearly rules out the possibility that it results from Co nanoparticles with an exchange-coupled CoO surface layer [64] formed in our sample. Since evidence for both FM and AF interactions between the doped ions were observed in $Zn_{0.88}Co_{0.12}O$, it may be possible that these interactions exist in different regions of the particles, thus producing an FM–AF interface. High-temperature magnetic measurements shown in figure 15 indicate a $T_c \sim 540$ K for $Zn_{0.88}Co_{0.12}O$, further confirming the novel FM behaviour developed in this sample. The 300 K hysteresis loop obtained after returning to room temperature following the T_c measurement still had a distinct open loop with a reduced coercivity, shown as an inset in figure 15. This rules out the possibility of any metastable FM phase of the type reported by Kundaliya *et al* [27] in Mn-doped ZnO being present in our $Zn_{0.88}Co_{0.12}O$ sample. It also shows that the magnetic transition at 540 K is the Curie temperature of the ferromagnetic $Zn_{0.88}Co_{0.12}O$ and not a structural/chemical phase transformation temperature.

4. Discussion

The various experimental results presented in section 3 clearly demonstrate that Co doping significantly changes the structural, morphological, optical and magnetic properties of ZnO. Up to ~3% Co, XRD, Raman spectroscopy, EPR spectroscopy and optical measurements strongly suggest that the Co ions substitute for the tetrahedral Zn^{2+} ions in ZnO lattice. Co doping clearly decreases the hexagonal crystallite growth and reduces the particle size with increasing Co concentration. XRD and optical measurements showed that the substitution of Co^{2+} in the Zn^{2+} sites is saturated for $x = 0.03$. For $x > 0.03$, XRD, Raman spectroscopy, XPS and optical data indicate that the additional Co ions occupy interstitial sites. Since interstitial incorporation of Co^{2+} occurs more easily on the particle surface due to the ease in obtaining an excess of oxygen ions, the particle size decreases (surface-to-volume ratio increases) for $x > 0.03$.

Proposals for the origin of ferromagnetism in TM-doped semiconductor oxides have been very controversial due to the reported presence of weaker secondary phases [66]. Careful

analysis using XRD, TEM, and selected-area electron diffraction, UV–vis spectrophotometry, Raman spectroscopy and EPR studies ruled out the presence of any phases other than wurtzite ZnO in the sample investigated in this work. The cobalt oxide sample prepared under identical synthesis conditions showed the formation of pure Co_3O_4, which is paramagnetic above its Néel temperature of 40 K [67]. None of the known oxides of Co are FM at room temperature. Furthermore, M versus T data obtained from the $Zn_{0.88}Co_{0.12}O$ did not show any peaks near 40 or 291 K, which correspond to the Néel temperatures of Co_3O_4 and CoO respectively. The systematic changes with increasing x in (i) the lattice parameters and particle size observed in XRD and TEM studies, (ii) the ZnO band gap and intensity of the Co^{2+} absorption edges in the optical measurements, and (iii) the Raman and PL peak position and intensity are all in strong support of the progressive incorporation of Co into the ZnO lattice with increasing x.

It is not completely clear what causes the $Zn_{0.88}Co_{0.12}O$ samples to develop an FM behaviour while such behaviour is absent in all the other samples prepared with $x < 0.12$ under identical conditions. The Co–Co distance certainly decreases with increasing Co concentration, and it is well known that magnetic interactions depend strongly on the spin–spin separation. However, the increasing Co concentration seems to produce a systematic increase in θ (figure 12), clearly suggesting that the dominant interaction between the Co spins is AF in nature and that its strength increases with x. The only anomalies that are observed as x approaches 0.12 is a rapid increase in the lattice parameters (figure 3(a)) and an increase in the oxygen content. Ferromagnetism induced by structural changes has been reported in itinerant electron metamagnets [68–70]; however, the possibility of such an origin for the observed ferromagnetism in $Zn_{0.88}Co_{0.12}O$ needs to be investigated further.

In a recent paper, Coey *et al* [71] proposed an FM exchange mechanism involving oxygen vacancies (□), which form F-centres with trapped electrons, for the observed ferromagnetism in TM-doped oxide semiconductors. Overlap of the F-centre electron orbitals with the d orbitals of the neighbouring TM spins to form TM–□–TM groups is crucial for the proposed FM coupling. Doped TM spins might also exist as isolated paramagnetic spin systems wherever the F-centre-mediated FM coupling is not achieved due to lack of TM neighbours and/or oxygen vacancies. Also, any TM–O^{2-}–TM superexchange interactions will be AF in nature. If this model is to be applied to the present system, it would indicate the formation of an almost stoichiometric $Zn_{1-x}Co_xO$ samples for $x \leqslant 0.10$ (to produce AF interacting Co spins) and a significant decrease in the oxygen content for $x = 0.12$ to develop the F-centre-mediated FM interaction in this sample. The carrier-mediated mechanism proposed by Sato and Yoshida [15–17] also favours electron doping (or oxygen vacancies) to produce ferromagnetism in ZnO through Co doping.

The Zn, Co and O concentration of the $Zn_{1-x}Co_xO$ samples obtained from the XPS spectra, shown in table 1, indicates that the oxygen content [O/(Zn + Co)] increases from 0.8 in pure ZnO to 0.9 in 2% Co-doped ZnO, while it is 1.1 for the 12% Co-doped sample. If our earlier conclusions that Co^{2+} ions are incorporated primarily at the substitutional Zn^{2+} sites for $x \leqslant 0.03$ and any further doping favours interstitial incorporation are true, the oxygen concentration should increase with x, especially for the $x > 0.03$ range. The observed ferromagnetism in the 12% Co-doped ZnO samples with [O/(Zn + Co)] > 1 and its complete absence in the oxygen-deficient samples are not in direct support of the electron-doping/oxygen-vacancy-mediated models.

Based on density function calculations, Risbud *et al* [30] have recently argued that $Zn_{1-x}Co_xO$ with p-type doping through Zn vacancies and/or excess oxygen could produce a stable ferromagnetic state. In contrast, they found that oxygen vacancies and the resulting n-type semiconductivity in $Zn_{1-x}Co_xO$ could stabilize an antiferromagnetic state. Our observation of ferromagnetism in Co-doped ZnO with [O/(Zn + Co)] > 1 as well as a

paramagnetic contribution with AF interaction (AF interaction parameter θ increases with x as shown in figure 13(b)) in all the other samples with $[O/(Zn + Co)] < 1$ are in qualitative agreement with the findings of Risbud *et al* [30]. In the 12% doped sample, the FM part may be dominant in the surface region where $[O/(Zn + Co)] > 1$ while the paramagnetic Co^{2+} ions with AF interaction might be occupying the core sites where $[O/(Zn + Co)] < 1$ based on the XPS data shown in table 1. The existence of such a ferromagnetic surface region and an antiferromagnetic core could produce an AF–FM interface within the individual particles, and this could explain the exchange bias observed in the $Zn_{0.88}Co_{0.12}O$ sample. These results, however, are different from those for Cr-doped indium tin oxide and Fe-doped tin dioxide systems recently reported by the authors [72, 73] where oxygen-deficient (and therefore an n-type behaviour) samples showed stronger ferromagnetism.

It should be noted that the changes observed in the oxygen concentration estimated from the XPS data are rather weak, and it is difficult to draw too strong conclusions without additional support. Therefore, more experimental investigations to determine the exact carrier type and concentration in the $Zn_{1-x}Co_xO$ samples, in relation to their magnetic properties, needs to be undertaken to confirm the above-mentioned possibilities. Such studies were difficult to carry out in the powder samples employed in this work, despite serious attempts. Efforts to observe the anomalous Hall effect and to understand the dependence of the FM properties, especially T_c, on the Co concentration, preparation temperatures, and the carrier concentration and type of the samples are needed to unambiguously determine the actual mechanism of the observed ferromagnetism [74].

5. Conclusions

Our detailed and systematic investigations carried out on sol–gel-synthesized nanoscale $Zn_{1-x}Co_xO$ samples with $0 \leqslant x \leqslant 0.12$ indicate that Co doping introduces significant changes in the lattice structure, particle size, morphology, band gap, and photoluminescence properties of ZnO along with changes in the magnetic behaviour. The major findings are the following.

 (i) For low doping levels ($x < 0.03$), tetrahedral Co^{2+} ions seem to be incorporated into the substitutional Zn^{2+} sites, as evidenced from XRD, Raman spectroscopy, diffuse reflectance spectroscopy, EPR, photoluminescence spectroscopy and XPS.
 (ii) Significant difference in the Co^{2+} incorporation process is observed for $x > 0.03$, as evidenced by the lattice expansion in XRD studies, changes in the Raman peak positions, saturation of the d–d crystal field transition intensities in diffuse reflectance, and saturation of the Co^{2+} EPR signal intensity. All these results can be qualitatively explained if Co^{2+} enters into interstitial sites in the ZnO host system.
(iii) Ferromagnetism is observed only in samples with a high 12% Co. XPS results indicate that for $x < 0.12$, the $Zn_{1-x}Co_xO$ samples are oxygen deficient while the $Zn_{0.88}Co_{0.12}O$ sample shows a slight excess of oxygen. This would indicate that n-type semiconductivity may not be a favourable condition to produce ferromagnetism in ZnO although additional experimental evidence is necessary to confirm this possibility.

Thus, Co doping acts as a method to tailor other physical properties of ZnO in addition to the possibility of introducing an FM behaviour, depending on the Co concentration.

Acknowledgments

References

[1] Özgür Ü, Teke A, Lui C, Cho S-J and Morkoç H 2004 *Appl. Phys. Lett.* **84** 3223
[2] Zu P, Tang Z K, Wong G K L, Kawasaki M, Ohtomo A, Koinuma K and Sagawa Y 1997 *Solid State Commun.* **103** 459
[3] Gruzintsev A N, Volkov V T and Yakimov E E 2003 *Semiconductors* **37** 259
[4] Hayashi H, Ishizaka A, Haemori M and Koinuma H 2003 *Appl. Phys. Lett.* **82** 1365
[5] Liu M, Kitai A H and Mascher P 1992 *J. Lumin.* **54** 35
[6] Sharma P, Sreenivas K and Rao K V 2003 *J. Appl. Phys.* **93** 3963
[7] Curri M L *et al* 2003 *Mater. Sci. Eng.* C **23** 285
[8] Kim H, Horwitz J S, Kim W H, Makinen A J, Kafafi Z H and Chrisey D B 2002 *Thin Solid Films* **420/421** 539
[9] Ohtaki M, Tsubota T, Eguchi K and Arai H 1996 *J. Appl. Phys.* **79** 1816
[10] Kutty T R N and Raghu N 1989 *Appl. Phys. Lett.* **54** 1796
[11] Chen M, Pei Z L, Sun C, Gong J, Huang R F and Wen L S 2001 *Mater. Sci. Eng.* B **85** 212
[12] Lee J, Lee H, Seo S and Park J 2001 *Thin Solid Films* **398/399** 641
[13] Dietl T, Ohno H and Matsukura F 2001 *Phys. Rev.* B **63** 195205
[14] Uspenski Yu, Kulatov E, Mariette H, Nakayama H and Ohta H 2003 *J. Magn. Magn. Mater.* **258/259** 248
[15] Sato K and Katayama-Yoshida H 2001 *Physica* B **308–310** 904
[16] Sato K and Katayama-Yoshida H 2002 *Phys. Status Solidi* b **229** 673
[17] Sato K and Katayama-Yoshida H 2002 *Semicond. Sci. Technol.* **17** 367
[18] Jalbout A F, Chen H and Whittenburg S L 2002 *Appl. Phys. Lett.* **81** 2217
[19] Ando K, Saito H, Jin Z, Fukumura T, Kawasaki M, Matsumoto Y and Koinuma H 2001 *Appl. Phys. Lett.* **78** 2700
[20] Makino T, Segawa Y, Kawasaki M, Ohtomo A, Shiroki R, Tamura K, Yasuda T and Koinuma H 2001 *Appl. Phys. Lett.* **78** 1237
[21] Lebedeva N and Kuivalainen P 2003 *J. Appl. Phys.* **93** 9845
[22] Ando K, Saito H, Jin Z, Fukumura T, Kawasaki M, Matsumoto Y and Koinuma H 2001 *J. Appl. Phys.* **89** 7284
[23] Ando K, Saito H, Jin Z, Fukumura T, Kawasaki M, Matsumoto Y and Koinuma H 2001 *Appl. Phys. Lett.* **78** 2700
[24] Rode K, Anane A, Mattana R, Contour J P, Durand O and LeBourgeois R 2003 *J. Appl. Phys.* **93** 7676
[25] Yang S G, Pakhomov A B, Hung S T and Wong C Y 2002 *IEEE Trans. Magn.* **38** 2877
[26] Pearton S J, Abernathy C R, Overberg M E, Thaler G T, Norton D P, Theodoropoulou N, Hebard A F, Park Y D, Ren F, Kim J and Boatner L A 2003 *J. Appl. Phys.* **93** 1
[27] Kundaliya D C, Ogale S B, Lofland S E, Dhar S, Metting C J, Shinde S R, Ma Z, Varughese B, Ramanujachary K V, Salamanca-Riba L and Venkatesan T 2004 *Nat. Mater.* **3** 709
[28] Pearton S J, Norton D P, Ip K, Heo Y W and Steiner T 2003 *Superlatt. Microstruct.* **34** 3
[29] Park J H, Kim M G, Jang H M, Ryu S and Kim Y M 2004 *Appl. Phys. Lett.* **84** 1338
[30] Risbud A S, Spaldin N A, Chen Z Q, Stemmer S and Seshadri R 2003 *Phys. Rev.* B **68** 205202
[31] Rao C N R and Deepak F L 2005 *J. Mater. Chem.* **15** 573
　　　Alaria J, Bieber H, Colis S, Schmerber G and Dinia A 2006 *Appl. Phys. Lett.* **88** 112503
[32] Hays J, Thurber A, Reddy K M, Punnoose A and Engelhard M H 2006 *J. Appl. Phys.* **99** 08M123
[33] Yan S, Ren C, Wang X, Xin Y, Zhou Z X, Mei L M, Ren M J, Chen Y X, Liu Y H and Garmestani H 2004 *Appl. Phys. Lett.* **84** 2376
[34] Mandal S K, Das A K, Nath T K, Karmakar D and Satpati B 2006 *J. Appl. Phys.* **100** 104315
[35] Yan L, Ong C K and Rao X S 2004 *J. Appl. Phys.* **96** 508
[36] Fouchet A, Prellier W, Padhan P, Simon Ch, Mercey B, Kulkarni V N and Venkatesan T 2004 *J. Appl. Phys.* **95** 7187
[37] Prellier W, Fouchet A, Mercey B, Simon C and Raveau B 2003 *Appl. Phys. Lett.* **82** 3490
[38] Schwartz D A, Norberg N S, Nguyen Q P, Parker J M and Gamelin D R 2003 *J. Am. Chem. Soc.* **125** 13205
[39] Ramachandran S, Tiwari A and Narayan J 2004 *Appl. Phys. Lett.* **84** 5255
[40] Venkatesan M, Fitzgerald C B, Lunney J G and Coey J M D 2004 *Phys. Rev. Lett.* **93** 177206

[41] Norton D P, Overberg M E, Pearton S J, Pruessner K, Budai J D, Boatner L A, Chisholm M F, Lee J S, Khim Z G, Park Y D and Wilson R G 2003 *Appl. Phys. Lett.* **83** 5488
[42] Yin Z, Chen N, Chai C and Yang F 2004 *J. Appl. Phys.* **96** 5093
[43] Kim K J and Park Y R 2002 *Appl. Phys. Lett.* **81** 1420
[44] Hays J, Punnoose A, Baldner R, Engelhard M H, Peloquin J and Reddy K M 2005 *Phys. Rev.* B **72** 075203
[45] Shannon R D and Prewitt C T 1969 *Acta Crystallogr.* B **25** 925
     Shannon R D 1976 *Acta Crystallogr.* A **32** 751
[46] Davis S R, Chadwick A V and Wright J D 1997 *J. Phys. Chem.* B **101** 9901
[47] Damen T C, Porto S P S and Tell B 1966 *Phys. Rev.* B **142** 570
[48] Jeong T S, Han M S, Youn C J and Park Y S 2004 *J. Appl. Phys.* **96** 175
[49] Schwartz D A, Norberg N S, Nguyen Q P, Parker J M and Gamelin D R 2003 *J. Am. Chem. Soc.* **125** 13205
[50] Dieguez A, Romano-Rodriguez A, Vila A and Morante J R 2001 *J. Appl. Phys.* **90** 1550
[51] Weakliem H A 1962 *J. Chem. Phys.* **36** 2117
[52] Kortum G 1969 *Reflectance Spectroscopy* (New York: Springer)
[53] Wang L and Giles N C 2003 *J. Appl. Phys.* **94** 973
[54] Schulz H-J and Thiede M 1987 *Phys. Rev.* B **35** 18
[55] Chambers S A, Farrow R F C, Maat S, Toney M F, Folks L, Catalano J G, Trainor T P and Brown G E Jr 2002 *J. Magn. Magn. Mater.* **246** 124
[56] Moulder J F, Stickle W F, Sobol P E and Bomben K D 1992 *Handbook of X-Ray Photoelectron Spectroscopy* (Eden Prairie, MN: Perkin-Elmer)
[57] Punnoose A, Hays J, Thurber A, Engelhard M H, Kukkadapu R K, Wang C, Shutthanandan V and Thevuthasan S 2005 *Phys. Rev.* B **72** 054402
     Punnoose A, Engelhard M H and Hays J 2006 *Solid State Commun.* **139** 434
[58] Jedrecy N, von Bardeleben H J, Zheng Y and Cantin J-L 2004 *Phys. Rev.* B **69** 041308
[59] Liu W K, Whitaker K M, Kittilstved K R and Gamelin D R 2006 *J. Am. Chem. Soc.* **128** 3910
[60] Heiman D, Shapira Y, Foner S, Khazai B, Kershaw R, Dwight K and Wold A 1984 *Phys. Rev.* B **29** 5634
[61] Punnoose A, Hays J, Gopal V and Shutthanandan V 2004 *Appl. Phys. Lett.* **85** 1559
[62] Manivannan A, Seehra M S, Majumder S B and Katiyar R S 2003 *Appl. Phys. Lett.* **83** 111
[63] Punnoose A, Seehra M, Shah N, Phanthavady T and Huffman G P 2004 *Phys. Rev.* B **69** 054425
[64] Meiklejohn W H and Bean C P 1956 *Phys. Rev.* **102** 1413
     Gruyters M and Riegel D 2000 *Phys. Rev.* B **63** 052401
[65] Seehra M S and Punnoose A 2004 *Solid State Commun.* **128** 299
     Punnoose A, Magnone H, Seehra M S and Bonevich J 2001 *Phys. Rev.* B **64** 174420
[66] Chambers S A and Farrow R F C 2003 *MRS Bull.* **28** 729
     Prellier W, Fouchet A and Mercey B 2003 *J. Phys.: Condens. Matter* **15** R1583
     Picozzi S 2004 *Nat. Mater.* **3** 349
[67] Lide D R *CRC Handbook of Chemistry and Physics* 84th edn (Boca Raton, FL: CRC Press) pp 12–125
[68] Duc N H and Goto T 1999 *Handbook on the Physics and Chemistry of Rare Earths* vol 26, ed K A Gschneidner and L Eyring (Amsterdam: Elsevier) p 178
[69] Goto T, Fukamichi K and Yamada H 2001 *Physica* B **300** 167
[70] Wohlfarth E P and Rhodes P 1962 *Phil. Mag.* **7** 1817
[71] Coey J M D, Douvalis A P, Fitzgerald C B and Venkatesan M 2004 *Appl. Phys. Lett.* **84** 1332
     Coey J M D, Venkatesan M and Fitzgerald C B 2005 *Nat. Mater* **4** 173
[72] Philip J, Punnoose A, Kim B I, Reddy K M, Layne S, Holmes J O, Satpati B, LeClair P R, Santos T S and Moodera J S 2006 *Nat. Mater.* **5** 298
[73] Misra S K, Andronenko S, Reddy K M, Hays J, Thurber A and Punnoose A 2007 *J. Appl. Phys.* **101** 09H120
[74] Dietl T 2001 *Acta Phys. Pol.* A **100** 139
     Dietl T 2002 *Semicond. Sci. Technol.* **17** 377
     Dietl T, Ohno H and Matsukura F 2001 *Phys. Rev.* B **63** 195205
     Dietl T, Ohno H, Matsukura F, Cibert J and Ferrand D 2000 *Science* **287** 1019